Scour and Burial Mechanics of Objects in the Nearshore

Scott A. Jenkins, Douglas L. Inman, Michael D. Richardson, Thomas F. Wever, and Joseph Wasyl

Abstract—**A process-based, numerical, hydrodynamic vortex lattice mine scour/burial model (VORTEX) is presented that simulates scour and burial of objects of arbitrary shape resting on a granular bed in the nearshore. There are two domains in the model formulation: a far-field where burial and exposure occur due to changes in the elevation of the seabed and a near-field involving scour and transport of sediment by the vortices shed from the object. The far-field burial mechanisms are based on changes in the equilibrium bottom profiles in response to seasonal changes in wave climate and accretion/erosion waves spawned by fluxes of sediment into the littoral cell. The near-field domain consists of one grid cell extracted from the far-field that is subdivided into a rectangular lattice of panels having sufficient resolution to define the shape of the object. The vortex field induced by the object is constructed from an assemblage of horseshoe vortices excited by local pressure gradients and shear over the lattice panels. The horseshoe vortices of each lattice panel release a pair of vortex filaments into the neighboring flow. The induced velocity of these trailing vortex filaments causes scour of the neighboring seabed and induces hydrodynamic forces on the object. Scour around the object and its subsequent movement into the scour depression contribute to burial, while far-field changes in local sand level may increase burial depth or expose the object. Scour and burial predictions of mines and mine-like objects were tested in field experiments conducted in the nearshore waters off the Pacific coast of California at Scripps Pier, the Gulf Coast of Florida at Indian Rocks, and off the Atlantic coast of Massachusetts at Martha's Vineyard. Model predictions of mine scour and burial are in reasonable agreement with field measurements and underwater photographs.**

Index Terms—**Cones, cylinders, fluid flow, hydrodynamics, mine burial, sediments.**

I. Introduction

SCOUR and scour marks are the erosional and accretionary bedform patterns that occur near objects that are on or near a sediment bed. Any form that locally concentrates vorticity near the bed can elevate bed shear stress and initiate onset of grain motion, leading to local bed scour including mounds and depressions on the bed itself. Once initiated, a pattern of scour may spread down current in the form of a growing field of current ripples, while vortex ripples under wave action may spread both against and with wave propagation from a single initiating irregularity in the bed [1]–[3].

Scour and burial of objects under unidirectional flow have been widely studied by engineers with an emphasis on piles of bridges and piers that protrude from the sediment bed, e.g., [4] and [5]. Scour is referred to as *local* when it results from the effects of structures on the flow pattern, *general* when it would occur irrespective of the presence of a structure, and is termed *clear water scour* when the bed upstream of the structure is at rest (e.g., [6]). In sedimentology, the interest has been directed toward the pattern of scour around individual objects, referred to as *scour marks* (e.g., [7] and [8]) or as *obstacle marks* [9], [10]. A recent review of scour and burial mechanics and nomenclature is given in [1].

There have been relatively few detailed studies of the scour and burial of mines, and the observations that have been made are separated by decades, with little intervening attention. A number of studies were carried out in the 1950s following World War II; e.g., Scripps Institution of Oceanography [11], Chesapeake Bay Institute [12], the U.S. Naval Electronics Laboratory [13], and Narragansett Marine Laboratory [14]–[16]. Although few studies were carried out during the Cold War, several studies were initiated following the Gulf War (e.g., [17]–[20]). A summary of mine burial studies and how their findings apply to present tactics is found in [21].

Observations show that burial is sensitive to the type of bottom sediment and the nature of the fluid forcing, and the size and shape of the object. Mines planted in areas of muddy sediments may sink upon impact and disappear into the mud. In contrast, mines planted in areas of sand, gravel, and rock undergo little burial upon impacting the bottom. This distinction has led to the two general categories of mine burial, *impact burial* and *subsequent burial*. This paper considers only the latter. Studies of mines placed on sandy bottoms show that subsequent burial occurs through a series of scour events followed by rolling or sliding of the mine into the scour depression [Fig. 1(a)]. However, burial can also result from net changes in the bottom elevation termed *far-field burial* [Fig. 1(b)]. Typically, far-field burial involves changes in the equilibrium bottom profiles associated with seasonal changes in wave climate [22]. High-energy winter waves cause erosion of the bar-berm portion of the profile, exposing mines close to shore, and accretion of the shorerise profile, causing burial of mines further offshore [Fig. 1(b)]. The reverse response can occur

Manuscript received April 15, 2005; revised June 28, 2006; accepted July 14, 2006. This work was supported by the U.S. Office of Naval Research under Coastal Geosciences Program Code 321 CG, with support from the Kavli Institute.

Guest Editor: R. H. Wilkens.

S. A. Jenkins and J. Wasyl are with the Marine Physical Laboratory, Scripps Institution of Oceanography, University of California at San Diego, La Jolla, CA 92093-0701 USA (e-mail: sjenkins@ucsd.edu; jwasyl@ucsd.edu).

D. L. Inman is with the Integrative Oceanography Division, Scripps Institution of Oceanography, University of California at San Diego, La Jolla, CA 92093-0209 USA (e-mail: dinman@ucsd.edu).

M. D. Richardson is with Marine Geosciences Division, Seafloor Sciences Branch, Naval Research Laboratory, Stennis Space Center, MS 39529-5004 USA (e-mail: mrichardson@nrlssc.navy.mil).

T. F. Wever is with the Forschunganstalt der Bundeswehr für Wasserschall und Geophysik (FWG), Kiel 24148, Germany (e-mail: ThomasWever@bwb.org).

Digital Object Identifier 10.1109/JOE.2007.890946

REPORT DOCUMENTATION PAGE

Form Approved
OMB No. 0704-0188

1. REPORT DATE *(DD-MM-YYYY)*	2. REPORT TYPE	3. DATES COVERED *(From - To)*
14072006	Journal Article	

4. TITLE AND SUBTITLE

Scour and Burial Mechanics of Objects in the Nearshore

5a. CONTRACT NUMBER

5b. GRANT NUMBER

5c. PROGRAM ELEMENT NUMBER

6. AUTHOR(S)

Scott A. Jenkins, Douglas L. Inman, Michael D. Richardson, Thomas F. Wever, Joseph Wasyl

5d. PROJECT NUMBER

5e. TASK NUMBER

5f. WORK UNIT NUMBER

7. PERFORMING ORGANIZATION NAME(S) AND ADDRESS(ES)

Naval Research Laboratory
Marine Geoacoustics Division
Stennis Space Center, MS 39529

8. PERFORMING ORGANIZATION REPORT NUMBER

NRL/JA/7430-06-7

9. SPONSORING/MONITORING AGENCY NAME(S) AND ADDRESS(ES)

Office of Naval Research
800 North Quincy Street
Arlington VA 22217-5000

10. SPONSOR/MONITOR'S ACRONYM(S)

ONR

11. SPONSOR/MONITOR'S REPORT

12. DISTRIBUTION/AVAILABILITY STATEMENT

Approved for public release; distribution is unlimite

13. SUPPLEMENTARY NOTES

IEEE Journal of Oceanic engineering, Vol. 32, No. 1, January 2007

14. ABSTRACT

Abstract—**A process-based, numerical, hydrodynamic vortex lattice mine scour/burial model (VORTEX) is presented that simulates scour and burial of objects of arbitrary shape resting on a granular bed in the nearshore. There are two domains in the model formulation: a far-field where burial and exposure occur due to changes in the elevation of the seabed and a near-field involving scour and transport of sediment by the vortices shed from the object. The far-field burial mechanisms are based on changes in the equilibrium bottom profiles in response to seasonal changes in wave climate and accretion/erosion waves spawned by fluxes of**

15. SUBJECT TERMS

Cones, cylinders, fluid flow, hydrodynamics, mine burial, sediments

16. SECURITY CLASSIFICATION OF:			17. LIMITATION OF ABSTRACT	18. NUMBER OF PAGES	19a. NAME OF RESPONSIBLE PERSON
a. REPORT	b. ABSTRACT	c. THIS PAGE			Michael Richardson
Unclassified	Unclassified	Unclassified	UU	13	19b. TELEPHONE NUMBER *(Include area code)* 228-688-4621

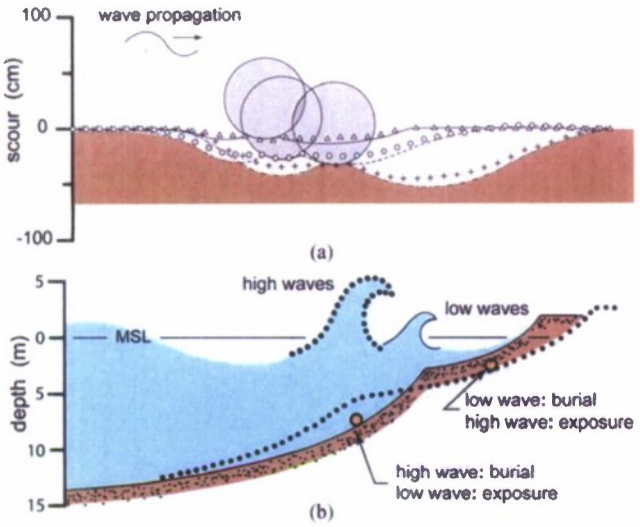

Fig. 1. Scour-burial mechanics: (a) near-field scour-roll burial sequence and (b) cyclical far-field burial exposure from seasonal profile change (from [21]).

with reestablishment of summer equilibrium beaches during periods of mild wave climate. In addition, the equilibrium profiles can shift on/offshore in response to divergence of drift or changes in the volume of littoral sediments as a consequence of river sediment yield and associated accretion/erosion wave phenomena [23].

II. Model

A. Architecture

Burial processes consist of two distinct types: near-field and far-field (Fig. 1). These operate on significantly different length and time scales. Near-field burial processes occur over length scales of the order of the mine dimensions and on time scales of a wave period, primarily governed by scour mechanics. In contrast, far-field processes involve changes in the elevation of the seabed with cross-shore distances of hundreds of meters that may extend along the coast for kilometers. Far-field time scales are typically seasonal with longer periods due to variations in climate and travel time of longshore sediment fluxes associated with accretion/erosion waves (e.g., [23]). These processes are coupled together in an architecture diagrammed by the flow chart shown in Fig. 2 and referred to as the *vortex lattice mine scour and burial model (VORTEX)* [11], [24].

The far-field processes and inputs are found above the orange line in Fig. 2 while the near-field processes and inputs are below the green line.

As with any boundary value problem, the solution follows from specifying initial conditions, forcing functions and the boundary conditions, from which the response is computed using a set of process-based algorithms. This computational sequence proceeds in Fig. 2 from the top down, with the set of forcing functions and initial conditions bundled together in a *module* shown by the pink shaded box at the top of the flow chart, while boundary conditions (beige box) and response (blue box) modules of the far-field are found in the pathways below that. The far-field response modules are upstream of the near-field modules in the computational flow chart because the far-field processes determine the fluid forcing and elevation of the sand bed around the object, essential to specifying the near-field boundary value problem.

The forcing function module (pink box) provides time series of waves (code #2), currents (code #3), and sediment flux (code #4). Waves and currents are derived either from direct observation [25], [26], or from forecast models such the National Oceanic and Atmospheric Administration (NOAA) wave watch (WW-III) model [25] or the U.S. Navy's distributed integrated ocean prediction system (DIOPS) [27]. The source for the flux of river sediment is based on the United States Geological Survey (USGS) monitoring data from its Hydrologic Benchmark Network and the National Stream Quality Accounting Network [28]. If these kinds of site-specific records are not available, then the forcing function module is configured to accept proxy records based on a geomorphic coastal classification system [21] represented by the orange shaded oval (code #1) in Fig. 2.

The wave and current forcing provides excitation applied to the deep water boundary of the far-field computational domain while the sediment flux is applied to the shoreline boundary. These boundaries are specified in the boundary conditions module (beige box) in Fig. 2, where the far-field computational domain is assembled from a series of boundary-conforming control cells (Fig. 3), using bathymetric data from the National Ocean Survey (NOS) and the USGS [28] as compiled by the National Geophysical Data Center [29].

With these forcing functions and boundary conditions, the far-field response module (blue box) computes the spatial and temporal evolution of the fluid forcing and bottom elevation along the cross-shore profiles of each control cell [Fig. 3(c)]. These cross-shore profiles are comprised of the following three matching segments: 1) the stationary profile that extends from the deep-water boundary inshore to closure depth h_c, where profile changes become vanishingly small, 2) the shorerise profile that continues from closure depth to the wave break point, and 3) the bar-berm profile that begins at the break point and ends at the berm crest. The stationary profile is invariant with time and is given by the regional bathymetry. Bottom elevation changes along the nonstationary profiles of the shorerise and bar-berm [Fig. 4(a)] are computed by code #10 in the far-field response module (blue box) using equilibrium profile algorithms after [30]–[34]. The stationary and nonstationary profiles are interpolated to create a Cartesian depth grid within each control cell on which simultaneous refraction and diffraction patterns are computed by code #6 using algorithms from [35] and [36] to specify fluid forcing by shoaling waves. Fluid forcing by currents in the far-field are computed in code #7 where wave-induced streaming and mass transport are based on algorithms after [37]–[39] and shallow-water tidal currents follow from algorithms after [40].

Fluid-forcing time series and bottom elevations computed in the far-field response module are throughput to the near-field response modules shown below the green line in Fig. 2. The far-field throughput is applied to the local seabed boundary conditions module (gray box). These local boundary conditions include the following two types: 1) the slope and the elevation

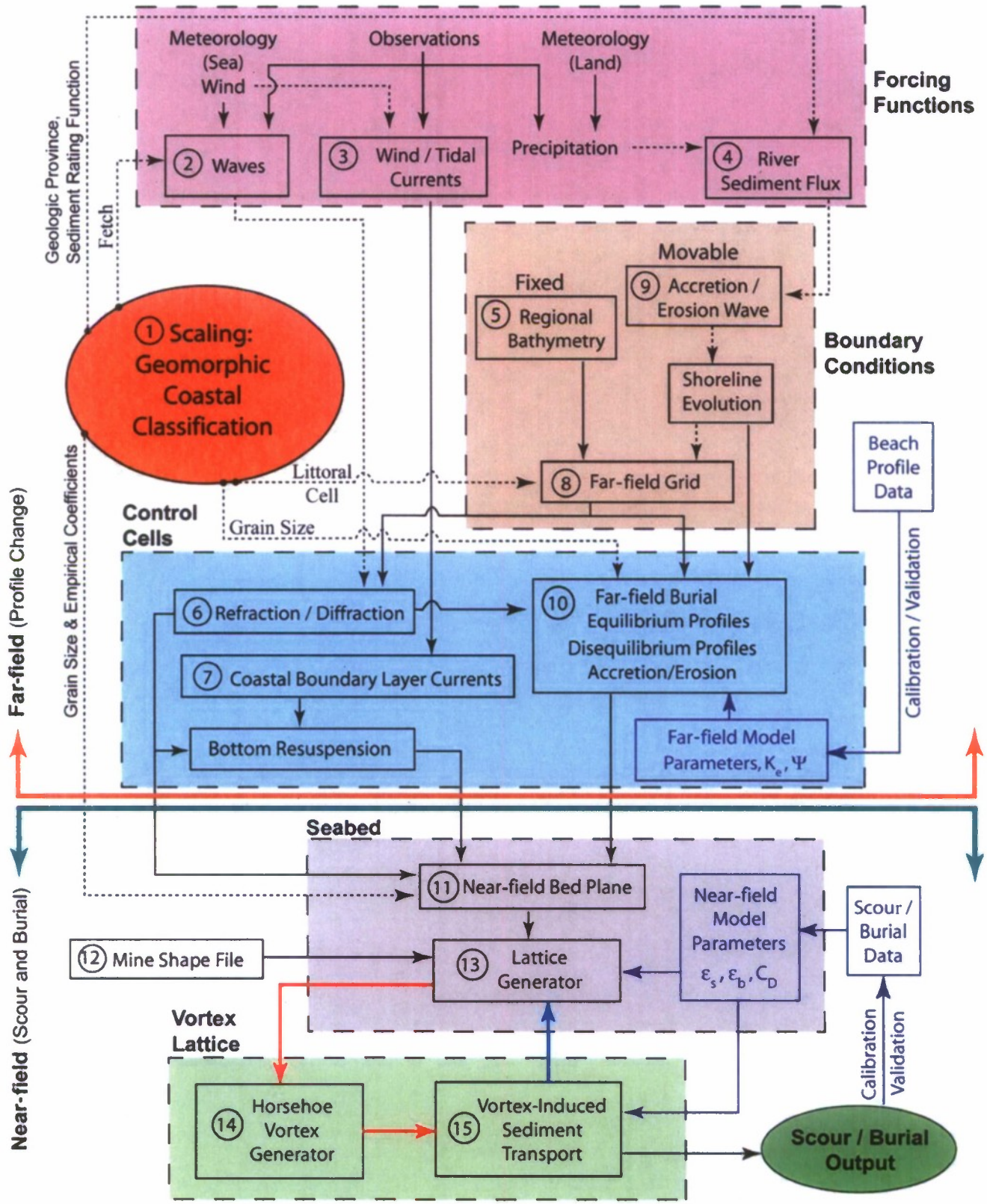

Fig. 2. Architecture of VORTEX.

of the seabed plane around the object base derived by code #11 from location in the far-field control cell and 2) the shape file of the mine in question (code #12). These two local boundary conditions are used to generate lattice panels by code #13

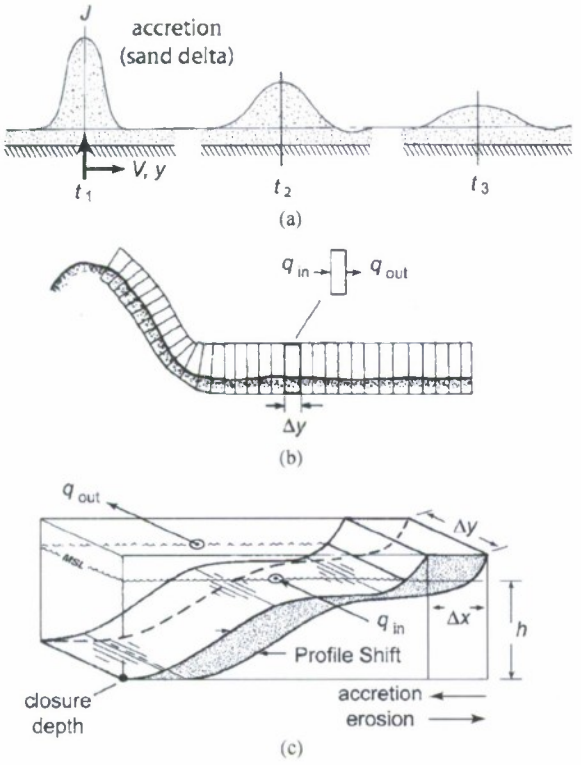

Fig. 3. Computational approach for modeling shoreline change (after [1]). (a) Accretion/erosion wave. (b) Coupled control cells. (c) Profile changes.

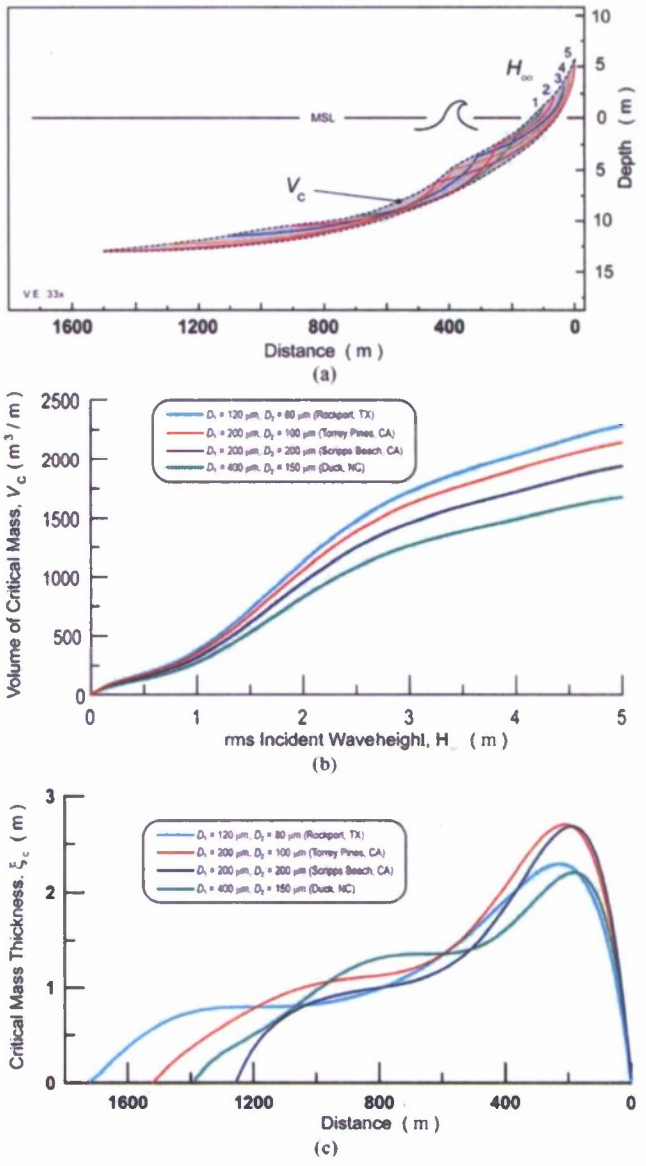

Fig. 4. Mechanics of far-field burial. (a) Envelope of profile change gives critical mass. (b) Volume of critical mass from elliptic cycloids. (c) Cross-shore variation in thickness.

that define the object and bedform of the surrounding seabed [Fig. 5(a)]. The lattice is the computational domain of the near-field scour-burial processes in which the method of the embedded vortex singularities (vortex lattice method) is applied in code #14 using algorithms after [41]–[43]. This method employs horseshoe vortices embedded in the near-bottom potential wave oscillation to drive local sediment transport in code #15 based on ideal granular bed load and suspended load equations after [44]–[46]. A horseshoe vortex is specified by code #14 for each lattice panel during every half-cycle of the wave oscillation as shown schematically in Fig. 5(a). The horseshoe vortices release trailing pairs of vortex filaments into the local potential flow field that induce downwash on the neighboring seabed [Fig. 6(b)], causing scour with associated bed and suspended load transport as computed by code #15. This scour action by trailing vortex filaments can be seen occurring in nature in Fig. 5(b).

The lattice generation in code #13, the horseshoe vortex generation in code #14, and the sediment transport computations in code #15 are implemented as a leapfrog iteration in a time-stepped loop shown by the red and blue pathway arrows at the bottom of Fig. 2. The leading time step (red arrow) computes the strength of the horseshoe vortex filaments generated by the pressure gradients and shear setup over the lattice panels of the combined body-bedform geometry of the previous (lagging) time step. The bed and suspended load transport induced by these filaments results in an erosion flux from certain neighboring lattice panels on the seabed and a deposition flux on others, based on image lifting line theory [Fig. 6(a)] as first applied in [47] to a mobile sedimentary boundary. The erosion and deposition fluxes of the leading time step are returned in the computational loop to the lattice generator (blue arrow) where those fluxes are superimposed on the lattice geometry of the lagging time step. That superposition produces a new lattice geometry for implementing the next leading time step. By this leapfrog iterative technique, an interactive bedform response is achieved whereby the flow field of the leading time step modifies the bedform of the lagging time step; and that modified bedform in turn alters the flow field of the next leading time step. This lead and lag arrangement is based on the fact that the inertial forces of granular bed near incipient motion are large compared to those of the fluid [44]; hence, the flow field responds faster to a change in bedform than the bedform can respond to a change in flow field.

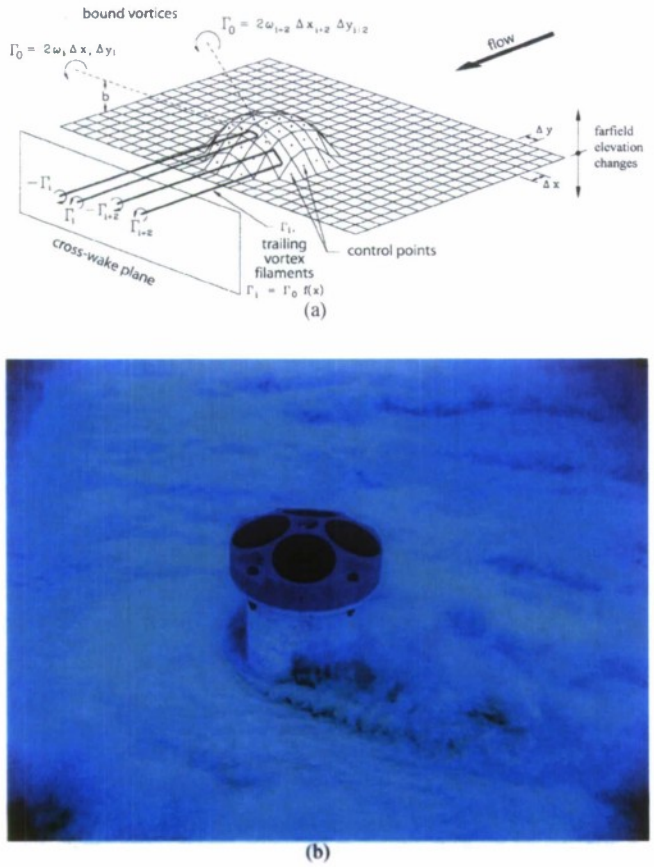

Fig. 5. Vortex lattice method. (a) Lattice and horseshoe vortex system. (b) Horseshoe vortices inducing sediment transport in nature (photo courtesy of K. Millikan).

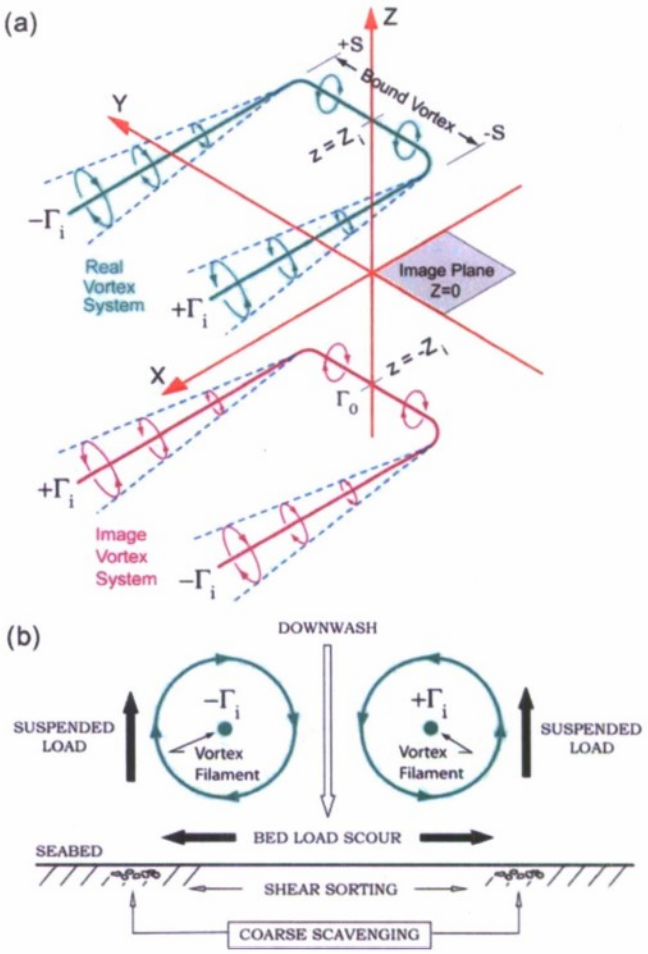

Fig. 6. (a) Image method for vortex-induced velocity at any point near the bed (image plane) due to the horseshoe vortex system of an arbitrary lattice panel [Fig. 5(a)]. The real vortex of the lattice panel is diagrammed in magenta and the image vortex is in green. (b) Schematic in the cross-wake plane of a pair of vortex filaments trailing out of the page [Fig. 5(a)].

B. *Far-Field Burial*

Far-field burial is controlled by broadscale changes in the nonstationary portion of the cross-shore profile located between closure depth and the berm-crest [Fig. 1(b)]. Here, the profile changes between various states of thermodynamic equilibrium that depend on incident waveheight H_∞, period T, sediment grain-size D, and littoral sediment volume V, as detailed in [34]. Variations in H_∞, T, and D cause the profile to change shape as shown in Fig. 4(a), while changes in local sediment volume ΔV will shift the profile either onshore ($\Delta V < 0$) or offshore ($\Delta V > 0$) as shown schematically in Fig. 3(c). The equilibrium profile for the shorerise ζ_2 and bar-berm ζ_1 segments of the nonstationary bathymetry are calculated from the elliptic cycloid solutions and closure depth relations in [34].

Integration of the elliptic cycloid equations over the range in wave climate gives a volume envelope containing all possible changes of the equilibrium profile, referred to as the *critical mass envelope*. The volume of the envelope applicable to mine burial will depend upon what is known about the time history of waves since the mines were deployed. When changes in waveheight are known or can be estimated, then the envelope will be for that range in waveheight. In Fig. 4(a), this volume of the critical mass envelope is shown as the gray-shaded region that envelopes all the equilibrium profiles for incident waveheights ranging $1\ \text{m} \leqslant H_\infty \leqslant 5\ \text{m}$. The critical mass envelope is calculated from the elliptic cycloid solutions ζ_1 and ζ_2 by

$$V_c = \iint \frac{\partial \zeta_1}{\partial H}\, dx dH + \iint \frac{\partial \zeta_2}{\partial H}\, dx dH \tag{1}$$

where x is the cross-shore coordinate taken positive in the offshore direction. When the integration in x is carried over the full length of the cycloids, V_c becomes approximately

$$V_c \cong 1.23 \times 10^{-4} (h_c)^{2.1} \left(\frac{H_\infty}{\Lambda}\right)^{0.9} \tag{2}$$

where

$$h_c = \frac{K_c H_\infty}{\sinh k h_c} \left(\frac{D_o}{D_2}\right)^{\psi}$$
$$\Lambda = 2^{2/5} H_\infty^{1/5} (\sigma^2/g\gamma)^{1/5}.$$

In (2), h_c is the closure depth as given by [34], ψ is a nondimensional empirical parameter, D_2 is the shorerise median grain size, D_o is a reference grain size, $\sigma = 2\pi/T$ is radian frequency, Λ is the shoaling factor relating breaker height to incident waveheight $\Lambda = H_\infty/H_b$ for a shoaling airy wave, g is acceleration

of gravity, and γ is a factor relating the depth of wave breaking h_b to breaker height $H_b = \gamma h_b$ with $K_e \sim 2.0, \psi \sim 0.33$, and $D_o \sim 100$ μm. Fig. 4(b) shows that the volume of sand contained in the critical mass envelope is a monotonically increasing function of the waveheight. Because the cycloid solutions also have grain-size dependence, there is a unique solution for the volume of critical mass for any arbitrary selection of the grain size in the bar-berm D_1 and the shorerise D_2. The application of critical mass is extended to a variety of coastal types by the choices of D_1 and D_2 in the curves shown in Fig. 4(b) and (c). Here, the sand size selections are proxies for several coastal types in the geomorphic coastal classification system [21] contained in code #1 of Fig. 2, including: marginal sea coast (Rockport, TX), collision coast (Torrey Pines and Scripps Beach, CA), and trailing-edge coast (Duck, NC).

Mines residing within the envelope of critical mass are subject to seasonal exposure and burial in accordance with wave climate variation. Mines that impact or scour below the critical mass envelope are permanently buried, while those planted seaward of the critical mass envelope, i.e., seaward of the closure depth, are subject only to gradual or partial burial by scour. The cross-shore thickness $\xi_c(x)$ of the seasonal critical mass envelope in Fig. 4(c) gives the maximum potential burial due to far-field processes at any arbitrary on/offshore location inshore of closure depth. When critical mass thickness exceeds the vertical dimension of a mine, $\xi_c(x)$ also determines the maximum burial depth, since scour processes vanish once the top of a mine matches the elevation of the seabed.

While the critical mass envelope accounts for far-field burial due to changes in shape of the equilibrium shorerise and bar-berm profiles, mines can also become buried by on/offshore shifts of those profiles associated with variation in the local volume of littoral sediment. The local sediment volume varies in response to the net change of the volume fluxes q between any given control cell and its neighbors, referred to as divergence of drift $= q_{\text{in}} - q_{\text{out}}$ [see Fig. 3(b) and (c)]. The mass balance of the control cell responds to a nonzero divergence of a drift with a compensating shift Δx in the position of the equilibrium profile [23], [48]. This is equivalent to a net change in the beach entropy of the equilibrium state [34]. The divergence of drift is given by the continuity equation of volume flux, requiring that dq/dt be the net of advective and diffusive fluxes of sediment plus the influx of new sediment J. The rate of the change of volume flux through the control cell causes the equilibrium profile to shift in time as

$$\Delta x(t) = \frac{1}{\Delta y(Z_1 + h_c)} \int \left[\frac{\partial}{\partial y} \left(\varepsilon \frac{\partial q}{\partial y} \right) - V \frac{\partial q}{\partial y} + J(t) \right] dt \tag{3}$$

where ε is the mass diffusivity, V is the longshore drift after [33], J is the flux of sediment from river sources, Δy is the alongshore length of the control cell, and Z_1 is the maximum run-up elevation from Hunt's formula [49]. River sediment yield J is calculated from streamflow Q, based on the power law formulation of that river's sediment rating curve after [50], or

$$J = \gamma Q^{\omega} \tag{4}$$

where γ and ω are empirically derived power law coefficients of the sediment rating curve from best fit (regression) analysis [50]. When river floods produce large episodic increases in J, a river delta is initially formed. Over time, the delta will widen and reduce in amplitude under the influence of surf diffusion and advect down-coast with the longshore drift, forming an accretion erosion wave [Fig. 3(a)] that can cyclically bury and reexpose mines as it propagates through the mine field [21], [23].

C. Near-Field Burial

Near-field burial is controlled by bedform changes associated with scour induced by the presence of the object. To simulate these bedform changes, the object and adjacent seabed is subdivided into a set of panels (*lattice*) as shown in Fig. 5(a). The vortex field induced by the object is constructed from an assemblage of horseshoe vortices, with a horseshoe vortex prescribed for each panel. This computational technique is known as the *vortex lattice method* and has been widely used in aerodynamics and naval architecture; see discussions in [41]. For any given ith panel in the lattice, the horseshoe vortex consists of a bound vortex Γ_o that contains all of the vorticity generated on the surface of a panel, and a pair of trailing vortex filaments $+\Gamma_i$ and $-\Gamma_i$ that discharge vorticity from the panel into the flow, causing a vertical wake. The trailing vortex filaments scrub the seabed and induce scour and suspension of bottom sediment as shown schematically in Figs. 5(a) and 6(b). For oscillatory flow, the vortex filaments must be specified for each half-cycle of motion.

The circulation of the vortex Γ_o, bound to the panel, is calculated from the boundary layer velocity shear [51], [52]

$$\Gamma_o = \int_0^{\delta} \int_{-S}^{S} \left\{ \Re \left(\frac{\partial \tilde{u}}{\partial z} \right)^2 \right\}^{1/2} dx dz \tag{5}$$

where δ is the boundary layer thickness, S is the half-width of the lattice panel, $\Re$ is the real part operator and the shear of the near-bottom flow, $\partial \tilde{u}/\partial z$, is prescribed from perturbation solutions for the wave/current boundary layer profile after [38], [39], [51]–[53] having the general analytic form

$$\begin{aligned} \tilde{u} = {} & u^{(1)} e^{i\sigma t} (1 - e^{-\alpha}) \\ & + u^{(2)} \left[\begin{array}{c} -\alpha e^{-\alpha *} + \left(1 - \frac{3}{2} i\right) e^{-\alpha *} - \frac{i}{2} e^{-\alpha} \\ + \left(\frac{i}{2} - \frac{1}{4}\right) e^{-2r/\delta} - \frac{3}{4} + \frac{3}{2} i \end{array} \right] \end{aligned} \tag{6}$$

where $u^{(1)}$ is the local oscillatory velocity amplitude from the potential flow at the top of the boundary layer $u^{(1)} = \nabla \phi$, and $u^{(2)} = 3\nabla (u^{(1)})^2 / 8\sigma$ is the steady streaming at the top of the boundary layer. The potential flow over the object $\nabla \phi$ is calculated using the method of tesseral harmonics forced by the local waveheight H_0 after [54] and [55]. Those solutions depend on the local refraction/diffraction results and elevation of the bed plane as throughput from the far-field response module and are repeated with each cycle through the near-field time-stepped loop (Fig. 2). The radian frequency of the wave oscillation is σ and the boundary layer profile is given by $\alpha = (1 + i) r/\delta$ in terms of the local surface normal coordinate r. Complex conjugates are denoted by an asterisk $(*)$.

The boundary layer thickness used to evaluate (5) and (6) is derived from [56] by finding for each panel the local solutions to the transcendental equation

$$\frac{30\delta}{Z_i}\log\left(\frac{30\delta}{Z_i}\right) = 1.2\left(\frac{d_0}{2Z_i}\right) \tag{7}$$

where Z_i is the elevation of the ith panel above the seabed and d_0 is twice the amplitude of the potential oscillation (orbital diameter) above the boundary layer. The factor d_0/Z_i in (7) accounts for lowest order inertial effects associated with the wave orbital velocity amplitude u_m as represented by the Keulegan–Carpenter number $N_{\mathrm{KC}} = u_m/\sigma L = d_0/(2Z_i)$ when the characteristic length scale is taken as $L \sim Z_i$.

The trailing vortices consist of right/left pairs whose circulation have equal but opposite rotation $+\Gamma_i$ versus $-\Gamma_i$ [Figs. 5(a) and 6(a)]. To prevent these vortices from inducing normal flow through the bottom plane, there is a set of image vortices beneath the bottom plane [Fig. 6(a)]. The mathematical representation of the trailing vortex filaments from a panel is derived from lifting line theory in ground effect according to [57] and [42]. Taking x as the stream-wise coordinate along the axis of wave propagation, y as the cross-stream component (parallel to the wave crests) and z measured vertically upward from the undisturbed seabed plane, the horseshoe vortex for the ith panel in the lattice is represented by

$$\begin{aligned}
\Gamma_i = &-\frac{\Gamma_o}{4\pi}\left\{\begin{array}{l}\tan^{-1}\left[\frac{(z-Z_i-b')(y+S)}{x\sqrt{x^2+(y+S)^2+(z-Z_i-b')^2}}\right]\\ -\tan^{-1}\left[\frac{(z+Z_i+b')(y+S)}{x\sqrt{x^2+(y+S)^2+(z+Z_i+b')^2}}\right]\end{array}\right\}\\
&-\frac{\Gamma_o}{4\pi}\left\{\tan^{-1}\left[\frac{(z+Z_i+b')(y-S)}{x\sqrt{x^2+(y-S)^2+(z+Z_i+b')^2}}\right]\right\}\\
&-\frac{\Gamma_o}{4\pi}\left\{\tan^{-1}\left[\frac{(z-Z_i-b')(y-S)}{x\sqrt{x^2+(y-S)^2+(z-Z_i-b')^2}}\right]\right\}\\
&-\frac{\Gamma_n}{4\pi}\left\{\tan^{-1}\left[\frac{(z+Z_i+b')}{(y-S)}\right]-\tan^{-1}\left[\frac{(z-Z_i-b')}{(y-S)}\right]\right\}\\
&-\frac{\Gamma_n}{4\pi}\left\{\begin{array}{l}\tan^{-1}\left[\frac{x(z+Z_i+b')}{(y-S)\sqrt{x^2+(y-S)^2+(z+Z_i+b')^2}}\right]\\ -\tan^{-1}\left[\frac{x(z-Z_i-b')}{(y-S)\sqrt{x^2+(y-S)^2+(z-Z_i-b')^2}}\right]\end{array}\right\}\\
&-\frac{\Gamma_n}{4\pi}\left\{\tan^{-1}\left[\frac{(z-Z_i-b')}{(y+S)}\right]-\tan^{-1}\left[\frac{(z+Z_i+b')}{(y+S)}\right]\right\}\\
&-\frac{\Gamma_n}{4\pi}\left\{\begin{array}{l}\tan^{-1}\left[\frac{x(z-Z_i-b')}{(y+S)\sqrt{x^2+(y+S)^2+(z-Z_i-b')^2}}\right]\\ -\tan^{-1}\left[\frac{x(z+Z_i+b')}{(y+S)\sqrt{x^2+(y+S)^2+(z+Z_i+b')^2}}\right]\end{array}\right\}
\end{aligned} \tag{8}$$

where b' is the displacement thickness representing the portion of the potential flow adjacent to the panel that must be indented to account for the singularity of the horseshoe vortex. The first three lines of (8) represent the bound vortex and its image; the next two lines are the $+\Gamma_i$ trailing vortex filament [right side of Fig. 6(b)] and its image, while the last two lines are the $-\Gamma_i$ trailing vortex filament [left side of Fig. 6(b)] and its image. As the pair of trailing vortex filaments extends downstream, the circulation Γ_n decreases due to diffusion of vorticity. This is represented schematically in Fig. 6(a) by the increasing diameters of the rotational paths. Mathematically, the decay of trailing vortex filaments in ground effect due to vorticity diffusion is prescribed by [43] as

$$\Gamma_n = \Gamma_o f(x) \tag{9}$$

where the perturbation series of the decay function can be written

$$f(x) = 1 - \frac{1}{u_m}\int_0^{N\Delta x}\left\{\begin{array}{l}u^{(1)} + u^{(2)}\left(\frac{x\sigma}{u_m S^2}\right)^{1/2}\\ +\left(\frac{x\sigma}{u_m S}\right)\left(u^{(1)} + S^2\frac{\partial^2 u^{(2)}}{\partial x^2}\right)\end{array}\right\}dx. \tag{10}$$

Here, N is the number of lattice panels. From [43], the displacement thickness b' in (8) can be approximated by

$$b' = \int_0^\infty\left(1 - \frac{\Gamma_o}{u\delta}\right)dz \cong 1.344\delta. \tag{11}$$

The release of trailing vortex filaments from each panel in Fig. 5(a) causes scour of the neighboring seabed. When viewed in any cross-wake plane [Fig. 6(b)] each pair of filaments induces a downwash flow that converges on the seabed and results in lateral bedload scour. Assuming ideal granular sediment transport physics after [44] and [45], the bedload scour transport rate is proportional to the cube of the vortex strength Γ_i, and inversely proportional to the cube of the grain-size D. Beyond the lateral extent of the bedload scour, the vortex filaments induce an upwashing flow of the suspended load, which for ideal granular sediments is proportional to Γ_i^4/D^4. Adopting the oscillatory waveform of the ideal granular transport relations from [46], the bedload scour rate for any given vortex filament (i-vortex) is given by

$$i_{bi} = \frac{\varepsilon_b C_D \rho \Gamma_i^3}{D^3(\tan\varphi - \tilde{u}\beta/|\tilde{u}|)} \tag{12}$$

while the suspended load scour is

$$i_{si} = \frac{\varepsilon_s C_D \rho \Gamma_i^3 |\Gamma_i|}{D^4(W_o - \tilde{u}\beta)} \tag{13}$$

where ε_b is the bedload transport efficiency, ε_s is the suspended load transport efficiency, C_D is the seabed drag coefficient which is a function of bed roughness, W_o is the settling velocity for any given sediment grain-size bin represented by a characteristic grain diameter D, and β is the local slope of the seabed.

The bed and suspended load transport rates from (12) and (13) are calculated every half-cycle of motion and summed over $N(t)$ number of lattice panels that make up the portion of the object above the seabed. The vortex-induced disturbance acting on the seabed is

$$\Gamma = \sum_i^{N(t)}\Gamma_i. \tag{14}$$

This disturbance generates increments of erosion and deposition flux, depending on the sign of (12) and (13), that are accumu-

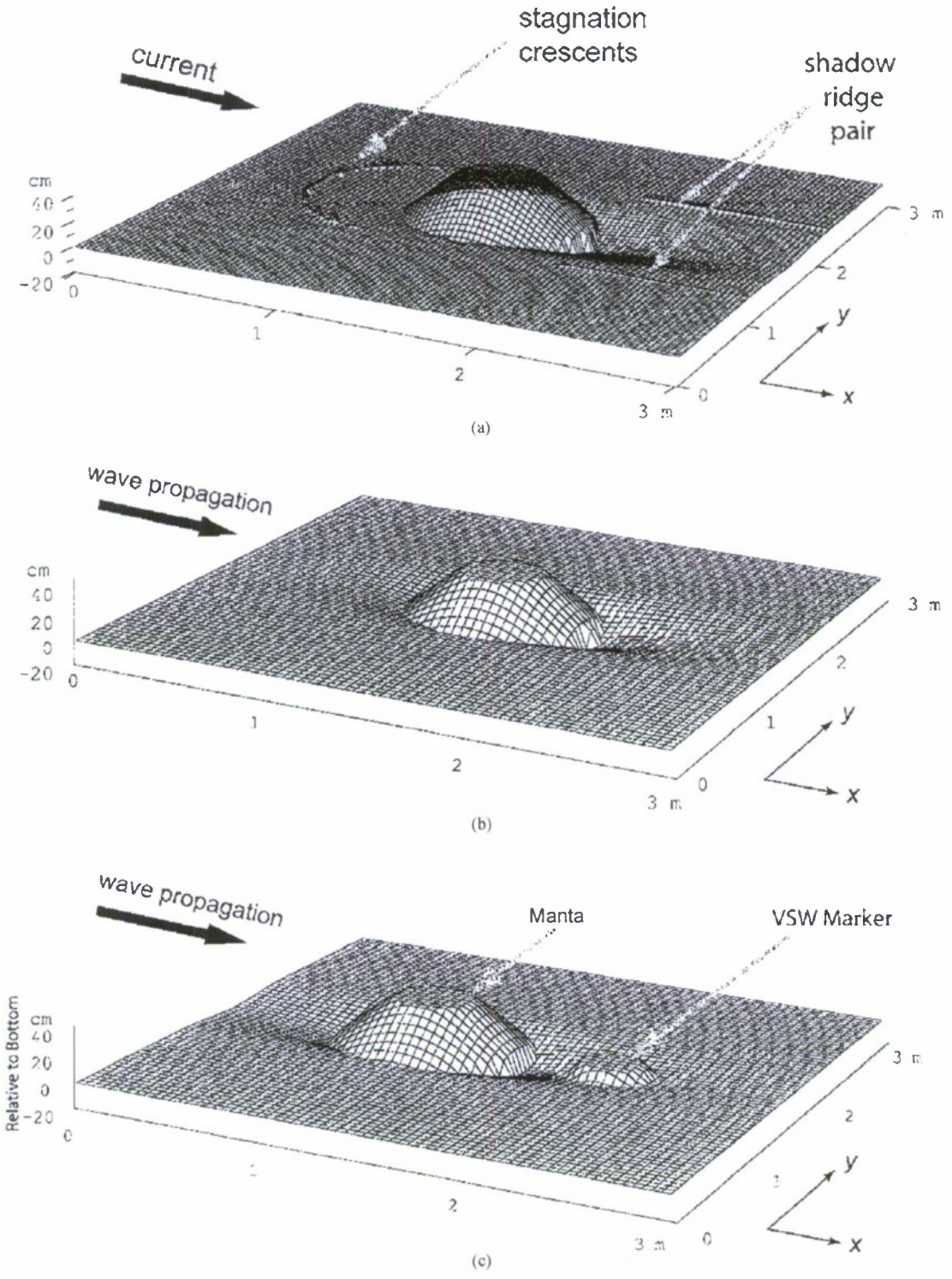

Fig. 7. Canonical scour patterns simulated by VORTEX model using frustums: (a) unidirectional current scour, (b) oscillatory wave scour, and (c) oscillatory wave scour with multiple interacting bodies.

lated each half-cycle of motion and mapped back into a revised lattice following the time-stepped loop diagrammed by red and blue pathways at the bottom of Fig. 2. The number of exposed lattice panels on the object $N(t)$ varies with each time step depending on the distribution of erosion and deposition fluxes over the lattice, and also with changes in the elevation of the seabed due to profile changes occurring in the far-field.

Simulations of scour produced by the vortex lattice method are shown in Fig. 7 for a body of revolution. This particular simulation is based on a frustum having the dimensions of a Manta

mine , with a base diameter of 98 cm, a top diameter of 43 cm, and a height of 43 cm. The grain size in each case was assumed to be 250 μm. In Fig. 7(a), steady currents of 40 cm/s produced an asymmetric bedform with a scour depression on the downstream side of the mine bounded by shadow ridge pairs. Bed accretion occurs on the upstream side of the mine where the approaching flow separates from the bed forming an arc of stagnation crescents. These are well-known features of current scour and obstacle marks found in river beds and desert dunes [7]. In Fig. 7(b), simulated scour due to oscillatory waves is found to be more symmetric for a frustum at 4-m depth under 1.25-m-high waves with a period of 10 s. The scour depression is slightly deeper on the down-waveside of the frustum where maximum scour depths are 14 cm as compared to 10 cm on the up-waveside. Similar wave-induced scour marks are found at the base of ocean pier piles and rocky outcrops in sandy shorezones [1], [9]. When the same wave conditions in Fig. 7(b) are superimposed on two frustums in close proximity as in Fig. 7(c), the simulated scour is significantly increased on both the up- and down-wavesides of the objects. The smaller of the two frustums in Fig. 7(c) has the dimensions of a very-shallow-water (VSW) marker (designed to neutralize the Manta mine). Despite its smaller size, the additional vortex filaments introduced by the VSW marker have increased maximum scour depths to 16 cm on both the up- and down-wavesides of the Manta. Enhancement of scour by two or more bodies in close proximity has been observed along the edges of cobble beds in otherwise sandy shorezones [1], [9], [10]. From these examples, it appears that the vortex lattice method when applied in ground effect over a bed of ideal granular sediment can make realistic 3-D simulations of scour for both unidirectional and oscillatory flows.

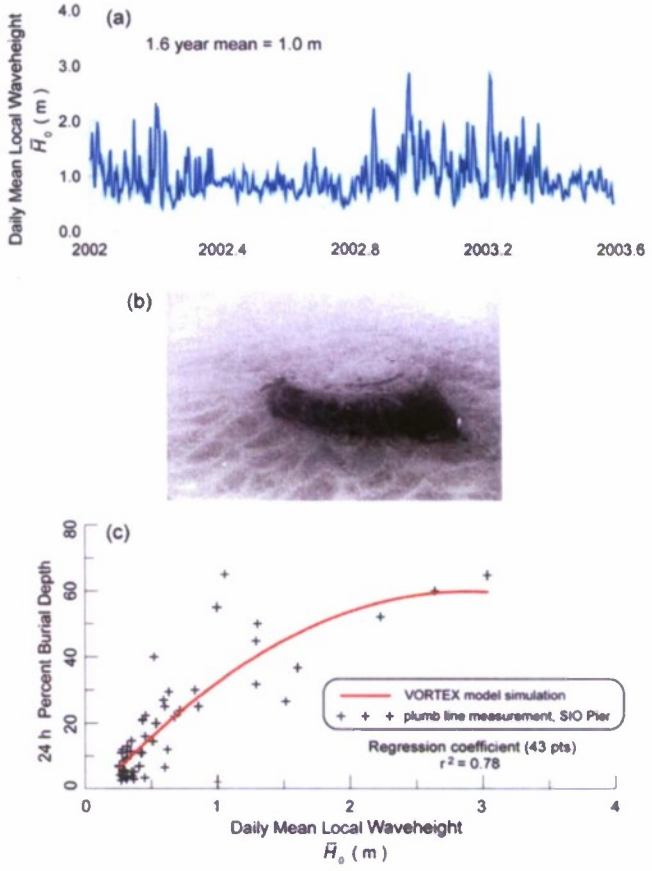

Fig. 8. Scripps Pier Manta mine burial experiments from 43 deployments: (a) daily mean local rms waveheight, (b) partially buried Manta mine at 6.1-m depth, and (c) 24-h percent burial depth from plumb line measurements (+) versus VORTEX model simulation.

III. Field-Validation Experiments

Field-validation experiments were conducted at three coastal environments in the geomorphic coastal classification system contained in code #1 of Fig. 2, namely: 1) a collision coast represented by the Scripps Pier site in La Jolla, CA, 2) a marginal sea coast represented by the Indian Rocks site off Tampa, FL, and 3) a trailing-edge coast represented by the Martha's Vineyard, MA. These sites provided examples of three of the five coastal types included in the geomorphic coastal classification system [21]. VORTEX model simulations at these sites used wave, current, grain size, and bathymetry data measured *in situ* to initialize the forcing functions and boundary conditions modules (Fig. 2). Free parameters used in the scour computations were based on published empirical estimates appropriate to the measured forcing, grain size, and bed roughness. The seabed drag coefficient C_D was based on the empirical relation of [58] and [59] while the bed and suspended transport efficiencies ε_b and ε_s were specified from [44] and [45].

A. Scripps Pier Experiments

The Scripps Pier experiments involved 43 deployments of a Manta mine at a 6.1-m depth between January 2002 and July 2003. Each deployment had 24-h duration during which time continuous wave monitoring was conducted by the coastal data information program (CDIP) [26]. The overhead boat hoist crane at the seaward end of Scripps Pier was used to deploy and recover the mine as well as measure burial depth. The boat hoist cable was fitted with a 100-lb weight that functioned as a plumb line after deployment of the mine. A pointer gage was fixed to the bottom end of the plumb line allowing the elevation of the top of the Manta to be precisely measured relative to the stationary pier deck. Plumb line measurements of mine elevation were performed immediately after deployment and again just before recovery 24 h later. The changes in the elevation of the mine between the two plumb line measurements gave an estimate of the subsidence of the mine. This simple scheme repeated 43 times during a 1.5-y period provided controlled measurements of burial for a defined sample interval in a variety of wave conditions including ten Pacific storms. During this period, the median grain size varied between 210 and 235μm. The nearest pier pile was 9.1 m away from the mine in a direction transverse to the wave propagation.

The variation in the local daily root-mean-square (rms) waveheight $\bar{H}_0$ during the deployment period is shown in Fig. 8(a), producing scour patterns during mild wave conditions ($H \sim$ 1 m) like those in Fig. 8(b) that qualitatively resemble the 3-D model simulation in Fig. 7(b). When burial depth is expressed as a percentage ratio of mine subsidence to the physical height of the mine, a monotonically increasing relationship is found between burial and daily rms waveheight over a 24-h period

[Fig. 8(c)]. The model simulation shown as the red line in Fig. 8 used fixed values for wave period and grain size ($T = 12$ s and $D = 225$ μm) that represented the mean values over the 1.5-y observational period. Despite the fact that period and grain size did vary among the 43 observations, the single-parameter relationship between waveheight and burial was found to provide useful information. The regression coefficient between measured burial and the single parameter burial simulation was found to be $r^2 = 0.78$, suggesting that simple *rule of thumb* relationships might be established between burial and waveheight, at least for short periods of time in shallow water.

B. Indian Rocks

The Indian Rocks Beach experiment utilized the acoustic instrumented mine (AIM) series of cylindrical mine shapes developed by the U.S. Naval Research Laboratory. With onboard acoustic and pressure sensors, this mine had self-recording capabilities for wave monitoring and burial depth. The particular mine used for comparisons to VORTEX model simulations was the AIM-3, measuring 2.032 m in length and 0.533 m in diameter [60], [61]. The AIM-3 was deployed at 15-m depth of water off Indian Rocks Beach, FL, where the seabed consisted of a well-sorted quartz sand having a median grain size of 133μm. Deployment occurred on January 8, 2003 and recovery on March 16, 2003. During that time, four traveling cold fronts crossed over the test site producing short period storm waves of up to 3-m local rms waveheight [60], [61].

Fig. 9(a) shows the continuous waveheight variation measured by the pressure sensor in the AIM-3 mine over the deployment period as reported by [61]. The storm waves from the four cold fronts are clearly evident. While maximum wave periods of 8 s were recorded during these storms, the mean wave period was typically only 5 s during the intervals of mild waves between the storms. This contrasts with the collision coast environment at Scripps Pier, where the shortest period storm waves were 8 s, the mean was 11 s, and the storm wave periods were 13–15 s. This contrast reflects the fetch limitations of a marginal sea environment. Because the near-field computations run on half-cycle time step intervals, these short period waves more than doubled the number of time steps required to run the VORTEX model at Indian Rocks.

The measured burial responses to the short period waves at Indian Rocks are shown in Fig. 9(b). Measurements from four individual AIM mines are compared here to the percent burial depth simulation of the VORTEX model that was derived from wave measurements by the AIM-3 mine. While the AIM measurements show continuous variation in burial, the VORTEX model simulates a series of episodic burial events coincident with the longer period storm waves. Furthermore, the AIM measurements show several cycles of partial reexposure that the VORTEX model totally misses. The suspected reason for this miss is the offshore location of the Indian Rocks test that is seaward of closure depth. Here, the far-field equilibrium profile algorithms of VORTEX that might otherwise predict reexposure fail to function. The broadscale bed elevation changes that occurred at Indian Rocks and led to the cyclical variation of burial in Fig. 9(b) were most likely due to current forcing [60], [61]. These currents were not included in the forcing function inputs

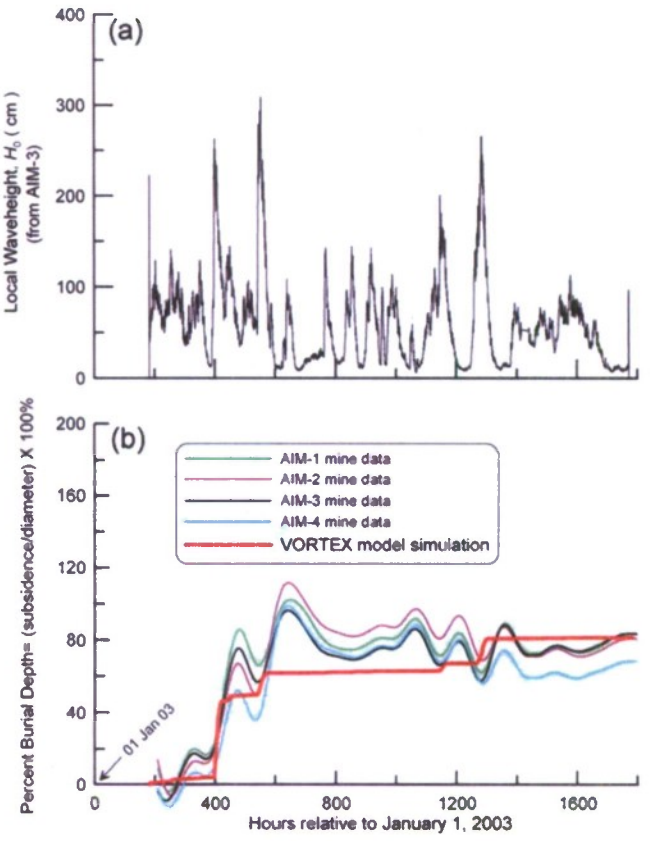

Fig. 9. Mine burial (based on subsidence below seabed plane) during Indian Rocks Beach experiment (January 8, 2003–March 16, 2003). (a) Waves over test site measured by AIM-3 mine. (b) Comparison of burial data versus VORTEX simulation of AIM-3.

to VORTEX. Regardless, the VORTEX simulation of burial for the AIM-3 mine is in close agreement with the data by the end of the deployment. Over the full length of the period of record, the regression coefficient between measured burial and burial simulation was found to be $r^2 = 0.83$.

In Fig. 10(a), an underwater photograph of the AIM-4 mine from [61] is compared with the VORTEX simulation of the scour/deposition pattern around the AIM-3 mine circa 1200 h into the deployment. Because the burial data of the AIM-4 and AIM-3 mines tend to track one another closely at this time in Fig. 9(b), the photograph is believed to be a reasonable proxy of the bedform around the AIM-3. The most notable feature in both the photograph and model simulation is the depositional ridge in the middle of the mine. This occurs because the induced velocity of the vortex ensemble over a cylinder on the seabed produces a net downwash in the middle of the cylinder (analogous to a wing) that promotes rapid settling and deposition of sediment that was scoured and suspended by the strong vortex filaments shed from the ends of the cylinder.

C. Martha's Vineyard

In the Martha's Vineyard experiment, the VORTEX model burial simulations were performed on the smaller self-recording cylindrical mine shape developed by the Forschungsanstalt der Bundeswehr für Wasserschall und Geophysik (FWG). These mines measure 1.5 m in length and 0.47 m in diameter [62].

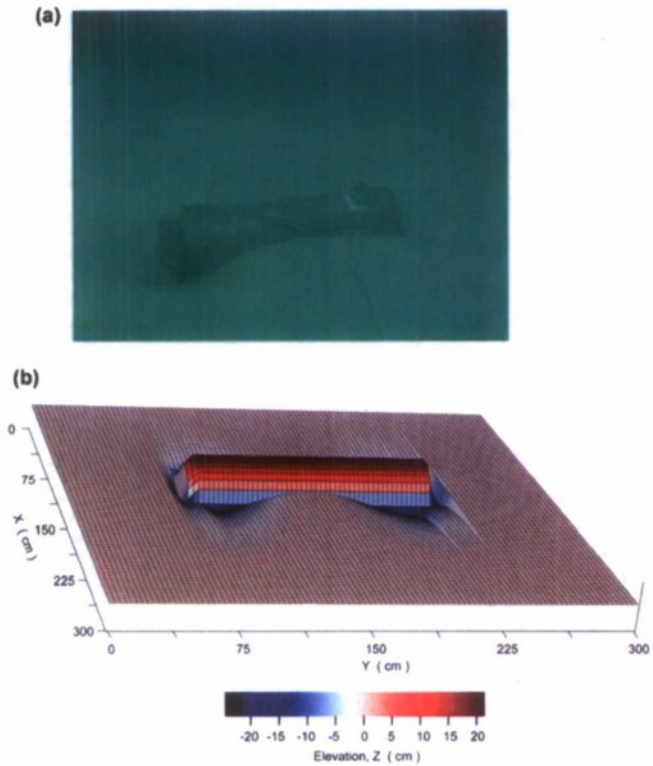

Fig. 10. Scour and deposition pattern around AIM mines at Indian Rocks, FL. (a) Diver photograph from [61]. (b) VORTEX model simulation.

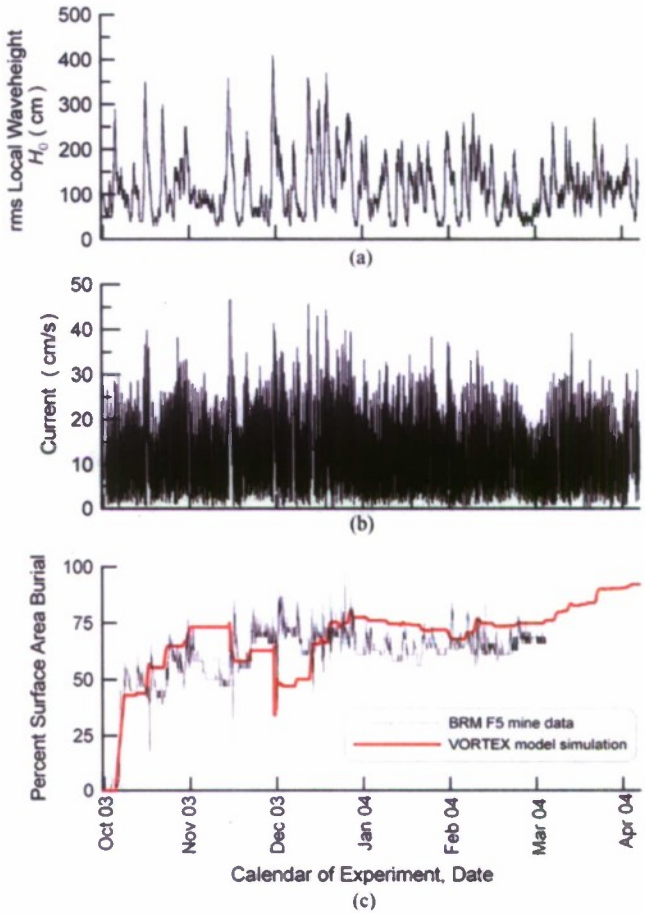

Fig. 11. Martha's Vineyard Coastal Observatory (MVCO, Edgartown, MA) mine burial measurements and simulation (Martha's Vineyard, September 30, 2003–April 6, 2004). (a) The rms local waveheight from [62]. (b) Current amplitude from [62]. (c) Percent of mine surface area buried (BRM-F5 self-registration mine data versus VORTEX model simulation).

Unlike the AIM mines, these mines utilized optical diodes rather than acoustic sensors to measure burial. Because of this, the FWG mines measure percent of surface area of the mine that is buried. The particular mine used for comparisons with the VORTEX model is the Boyevaya Mashina Pekhoty (BRM)-F5 mine deployed on October 1, 2003 at the 12-m depth of water on a coarse sand bottom with median diameter estimated to be 450 μm. The mine was aligned in an east-west direction, generally parallel to the crests of incident waves from the south–south–east (SSE). Due to a build up of barnacles, over its optical diodes it ceased functioning on March 2, 2004.

The VORTEX model was initialized with high-resolution bathymetry obtained from the multibeam sonar scans of the test site just before deployment of the mines. Wave and current forcing for the model was derived from *in situ* measurements by the Martha's Vineyard Coastal Observatory (MVOC), [62]. The waveheight record during the deployment from [63] is shown in Fig. 11(a) and the amplitudes of the predominant tidal currents are in Fig. 11(b). It is apparent from Fig. 11(a) that a high-energy wave climate prevailed at the Martha's Vineyard test site, particularly during the first half of the experiment (October 2003–January 2004). A total of 27 storms produced waves at the 10-m water depth with significant waveheights greater than 2 m. Of those 27 storms, seven produced local rms waveheights exceeding 3 m. Superimposed on these storm waves were tidal currents averaging 25 cm/s with spring tide maximums exceeding 40 cm/s [Fig. 11(b)].

To make comparisons with the BRM-F5 burial data VORTEX was configured to write a running count of the number of lattice panels that were buried after each time step. A comparison between measurements and simulation of the percentage of the total surface area of the mine that became buried is shown in Fig. 11(c). Both the observations and the simulation show that the mine became rapidly buried with the early onset of the winter storm waves. Thereafter, burial proceeded more slowly as only about 25% of the mine surface area produced any disturbance to the ambient flow. While the data and model simulation are at variance by as much as 25% surface-area burial during certain intervals of the experiment, the regression coefficient taken over the entire period of record is nonetheless $r^2 = 0.88$.

IV. Conclusion

A numerical model has been developed that simulates the scour and burial of objects on the seabed based on far-field formulations of bottom elevation change and near-field formulations of bedform change using vortex lattice methods in an image system. While the model is computationally intensive, requires rather extensive input files, and is disadvantaged by long computational run times, it is capable of realistic 3-D simulations of the scour field for a variety of body geometries and flow conditions, including both steady and complex peri-

odic motion (Figs. 1, 7, and 10). The model contains far-field burial algorithms that can predict both burial and exposure due to broadscale changes in the nearshore bathymetry as a consequence of wave climate and the variability of littoral sediment supply. This allows the model to map out regions of the nearshore where cyclical burial/exposure is likely and quantify the degree of such burial/exposure as a function of a specific location in the nearshore. The model can also be used in sensitivity analyses to evaluate which forcing functions and boundary conditions exert a leading order effect on scour and burial (Fig. 8). The model was tested in the following three distinct coastal types: a collision coast in the Southern California Bight, a marginal sea coast in the Gulf of Mexico, and a trailing-edge coast in New England. The regression coefficients between measured burial and model simulation ranged $0.78 \leqslant r^2 \leqslant 0.88$, with the poorest results occurring when an incomplete set of forcing functions was provided to the model.

REFERENCES

[1] D. L. Inman and S. A. Jenkins, "Scour and burial of objects in shallow water," in *Encyclopedia of Coastal Science*, M. Schwartz, Ed. Dordrecht, The Netherlands: Springer-Verlag, 2005, pp. 825–830.

[2] D. L. Inman and A. J. Bowen, "Flume experiments on sand transport by waves and currents," in *Proc. 8th Conf. Coast. Eng.*, San Diego, CA, 1962, pp. 137–150.

[3] E. B. Tunstall and D. L. Inman, "Vortex generation by oscillatory flow over rippled surfaces," *J. Geophys. Res.*, vol. 80, no. 24, pp. 3475–3484, Aug. 1975.

[4] T. J. Collins, "Investigating bridge scour," *Railway Track Structure*, p. 76, 1980.

[5] Y. M. Chiew and B. W. Melville, "Local scour around bridge piers," *J. Hydraulic Res.*, vol. 25, pp. 15–26, 1987.

[6] A. J. Raudkivi, *Loose Boundary Hydraulics*. New York: Pergamon, 1990.

[7] F. J. Pettijohn and P. E. Potter, *Atlas and Glossary of Primary Sedimentary Structures*. New York: Springer-Verlag, 1964.

[8] H.-E. Reineck and I. B. Singh, *Depositional Sedimentary Environments.*. New York: Springer-Verlag, 1975.

[9] J. R. L. Allen, *Sedimentary Structures, Their Character and Physical Basis*. Amsterdam, The Netherlands: Elsevier, 1984.

[10] J. R. L. Allen, *Principles of Physical Sedimentology*. London, U.K.: G. Allen, 1985.

[11] D. L. Inman and S. A. Jenkins, "A chronology of ground mine studies and scour modeling in the vicinity of La Jolla," Scripps Inst. Oceanogr., Univ. California, La Jolla, CA, SIO Ref. Ser. 96-13, 1996.

[12] W. V. Burt, M. C. Powers, and D. W. Pritchard, "Operation mud—results of studies of mine penetration in the York River," Chesapeake Bay Inst., Johns Hopkins Univ., Ref. No. 52-25, 1952.

[13] R. F. Dill, "The burial and scouring of ground mines on a sandy bottom," U. S. Navy Electron. Lab., San Diego, CA, Res. Rep. NEL 861, 1958.

[14] J. J. Donohue and L. E. Garrison, "An evaluation of mine behavior observations in four test areas," Narragansett Marine Lab., Univ. Rhode Island, Narragansett, RI, Ref. No. 54-13, 1954.

[15] R. L. McMaster, L. E. Garrison, and S. D. Hicks, "Marine sedimentation project; mine behavior studies," Narragansett Marine Lab., Univ. Rhode Island, Narragansett, RI, Ref. No. 55-15, 1955.

[16] D. E. Frazier and C. E. Miller, "Geological and engineering characteristics at mine behavior test sites," Narragansett Marine Lab., Univ. Rhode Island, Narragansett, RI, Ref. No. 55-16, 1955.

[17] D. Foxwell, "New technology takes on the sea mine," *Int. Defense Rev.*, pp. 1097-99–1101-1102, Oct. 1991.

[18] P. J. Mulhearn, "Experiment on mine burial by scour," Materials Res. Lab., Maribyrnong, Vic., Australia, MRL-TN-632, 1993.

[19] P. J. Mulhearn, "Experiments on mine burial on impact-Sydney Harbour," *U. S. Navy J. Underwater Acoust.*, vol. 43, no. 3, pp. 1271–1281, Jul. 1993.

[20] P. C. Chu, A. F. Gilles, C. Fan, and P. Fleischer, "Hydrodynamics of falling mine in water column," in *Proc. J. Counter-Ordnance Tech. 5th Int. Symp. Tech. Mine Problem*, 2002, pp. 100–108 [Online]. Available: http://www.demine.org/SCOT/Papers/pdfpapers.html

[21] D. L. Inman and S. A. Jenkins, "Scour and burial of bottom mines—A primer for fleet use," Scripps Inst. Oceanogr., Univ. California, San Diego, CA, SIO Ref. Ser. 02-8, 2002 [Online]. Available: http://repositories.cdlib.org/sio/reference/02-8/

[22] D. L. Inman, M. H. S. Elwany, and S. A. Jenkins, "Shorerise and barberm profiles on ocean beaches," *J. Geophys. Res.*, vol. 98, no. C10, pp. 18 181–18 199, Oct. 1993 [Online]. Available: http://repositories.cdlib.org/sio/cmg/11/

[23] D. L. Inman and S. A. Jenkins, "Accretion and erosion waves on beaches," in *Encyclopedia of Coastal Science*, M. Schwartz, Ed. Dordrecht, The Netherlands: Springer-Verlag, 2005, pp. 1–4 [Online]. Available: http://repositories.cdlib.org/sio/cmg/6/

[24] S. A. Jenkins and D. L. Inman, "Model for mine scour and burial: An illustrated abstract with technical appendix," Scripps Inst. Oceanogr., Univ. California, San Diego, CA, SIO Ref. Ser. 02-2, 2002.

[25] National Oceanic and Atmospheric Association (NOAA), Nat. Data Buoy Ctr., 2003 [Online]. Available: http://ndbc.noaa.gov/

[26] Scripps Institution of Oceanography, University of California, "Coastal data information program," SIO Ref. Ser. 01-20, 2006 [Online]. Available: http://cdip.ucsd.edu

[27] Oceanographic and Atmospheric Master Library (OAML) 2004 [Online]. Available: http://navy.ncdc.noaa.gov/products/oaml.html

[28] United States Geological Survey (USGS), "National water information system: Web interface," 2006 [Online]. Available: http://waterdata.usgs.gov/nwis/

[29] National Geophysical Data Center (NGDC) 2006 [Online]. Available: http://www.ngdc.noaa.gov/mgg/gdas/gd_designagrid.html

[30] C. E. Nordstrom and D. L. Inman, "Sand level changes on Torrey Pines Beach," U.S. Army Corps Eng., Coast. Eng. Res. Ctr., Miscellaneous Paper 11-75, 1975.

[31] D. L. Inman, "Areal and seasonal variations in beach and nearshore sediments at La Jolla," U.S. Army Corps Eng., Beach Erosion Board, Tech. Memorandum 39, 1953.

[32] D. L. Inman and T. K. Chamberlain, "Particle size distribution in nearshore sediments," in *Proc. Soc. Econom. Paleontologists and Mineralogists Symp. Finding Ancient Shorelines*, 1955, pp. 106–129, Special Publication 003.

[33] D. K. Stauble, "Long-term profile morphodynamics: Field research facility case history," U.S. Army Coast. Eng. Res. Ctr., Tech. Rep. CERC-92-7, 1992.

[34] S. A. Jenkins and D. L. Inman, "Thermodynamic solutions for equilibrium beach profiles," *J. Geophys. Res.*, vol. 111, pp. 1–21, 2006, doi:10.1029/2005JC002899.

[35] J. T. Kirby, "Higher-order approximations in the parabolic equation method for water-waves," *J. Geophys. Res.*, vol. 91, no. C1, pp. 933–952, 1986.

[36] R. A. Dalrymple, J. T. Kirby, and P. A. Hwang, "Wave diffraction due to areas of energy dissipation," *J. Waterway Port, Coast, Ocean Eng.*, vol. 110, pp. 67–79, 1984.

[37] M. S. Longuet-Higgins, "Mass transport in water waves," *Philos. Trans. Roy. Soc. London A, Math Phys. Sci.*, vol. 245, pp. 535–581, 1953.

[38] J. Lamoure and C. C. Mei, "Effects of horizontally 2-dimensional bodies on mass-transport near sea bottom," *J. Fluid Mech.*, vol. 83, no. 3, pp. 415–433, 1977.

[39] M. S. Longuet-Higgins, "Steady currents induced by oscillations around islands," *J. Fluid Mech.*, vol. 42, no. 4, pp. 701–720, 1970.

[40] J. J. Connor and J. D. Wang, "Finite element modeling of two-dimensional hydrodynamic circulation," MIT, Cambridge, MA, Tech. Rep. MITSG 74-4, 1973, pp. 1–57.

[41] B. W. McCormick, *Aerodynamics, Aeronautics, and Flight Mechanics*. New York: Wiley, 1979.

[42] M. Van Dyke, *Perturbation Methods in Fluid Mechanics*. Stanford, CA: Parabolic, 1975, p. 271.

[43] A. J. Peace and N. Riley, "A viscous vortex pair in ground effect," *J. Fluid Mech.*, vol. 129, pp. 409–426, Apr. 1983.

[44] R. A. Bagnold, "The flow of cohesionless grains in fluids," *Philos. Trans. Roy. Soc. London A, Math Phys. Sci.*, vol. 249, no. 964, pp. 235–297, 1956.

[45] R. A. Bagnold, "Mechanics of marine sedimentation," in *The Sea, Ideas and Observations on Progress in the Study of the Seas*, M. N. Hill, Ed. New York: Wiley, 1963, vol. 3, The Earth Beneath the Sea, History, pp. 507–528.

[46] A. J. Bowen, S. B. McCann, Ed., "Simple models of nearshore sedimentation: Beach profiles and longshore bars," *The Coastline of Canada: Littoral Processes and Shore Morphology*, pp. 1–11, 1980, Paper 80-10.

[47] S. A. Jenkins and J. Wasyl, "Resuspension of estuarial fine sediments by tethered wings," *J. Coast. Res.*, vol. 6, no. 4, pp. 961–980, 1990.
[48] D. L. Inman and R. Dolan, "The outer banks of North Carolina: Budget of sediment and inlet dynamics along a migrating barrier system," *J. Coast. Res.*, vol. 5, no. 2, pp. 193–237, 1989.
[49] I. A. Hunt Jr., "Design of seawalls and breakwaters," *J. Waterways, Harbors, Coast. Eng. Div.*, vol. 85, pp. 123–152, 1959.
[50] D. L. Inman and S. A. Jenkins, "Climate change and the episodicity of sediment flux of small California rivers," *J. Geology*, vol. 107, no. 3, pp. 251–270, May 1999 [Online]. Available: http://repositories.cdlib.org/sio/cmg/2/
[51] S. A. Jenkins and D. L. Inman, "On a submerged sphere in a viscous fluid excited by small-amplitude periodic motions," *J. Fluid Mech.*, vol. 157, pp. 199–224, 1985.
[52] G. K. Batchelor, *An Introduction to Fluid Mechanics*.. Cambridge, U.K.: Cambridge Univ. Press, 1970.
[53] M. S. Longuet-Higgins, "Longshore currents generated by obliquely incident waves, I," *J. Geophys. Res.*, vol. 75, no. 33, pp. 6778–6789, 1970.
[54] T. H. Havelock, "The pressure of water waves upon a fixed obstacle," in *Proc. R. Soc. Lond. A, Math. Phys. Sci.*, 1940, vol. 175, pp. 409–421.
[55] T. H. Havelock, "The moment on a submerged solid of revolution moving horizontally," *Quart. J., Mech. Appl. Math*, vol. 5, pp. 129–136, 1952.
[56] I. G. Jonsson and N. A. Carlsen, "Experimental and theoretical investigations in an oscillatory turbulent boundary layer," *J. Hydraulic Res.*, vol. 14, no. 1, pp. 45–60, 1976.
[57] M. Van Dyke, "Lifting-line theory as a singular-perturbation problem," *J. Appl. Math. Mech.*, vol. 28, pp. 90–102, 1964.
[58] K. Kajiura, "A model of the bottom boundary layer in water waves," *Bull. Earthquake Res. Inst. (Tokyo)*, vol. 46, pp. 75–123, 1968.
[59] G. I. Taylor, "Note on R. A. Bagnold's empirical formula for the critical water motion corresponding with the first disturbance of grains on a flat surface," in *Proc. R. Soc. Lond. A, Math. Phys. Sci.*, 1946, vol. 187, no. 1008, pp. 16–18.
[60] G. R. Bower, M. D. Richardson, K. B. Briggs, P. A. Elmore, E. F. Braithwaite III, J. Bradley, S. Griffin, T. F. Waver, and R. Lühder, "Measured and predicted burial of cylinders during Indian Rocks Beach Experiment," *IEEE J. Ocean. Eng.*, vol. 32, no. 1, pp. 91–102, Jan. 2007.
[61] G. R. Bower, M. D. Richardson, K. B. Briggs, W. C. Vaughan, C. S. Kennedy, E. F. Braithwaite III, S. Griffin, J. Bradley, T. F. Wever, and R. Lühder, "Indian Rocks Beach Experiment January–March 2003," U.S. Naval Res. Lab., Washington, DC, NRL/MR/7430–04-8752, 2004, p. 103.
[62] Woods Hole Oceanographic Institution, "Martha's Vineyard Coastal Observatory (MVCO)," Woods Hole, MA, 2006 [Online]. Available: http://mvcodata.whoi.edu/cgi-bin/mvco/mvco.cgi
[63] T. F. Wever and R. Lühder, "Mine burial monitoring by the FWG burial registration mines during 2003/2004 ONR mine burial prediction experiment at Martha's Vineyard Coastal Observatory," Kiel, Germany, Tech. Rep. TB 2004-20, 2004, p. 50.

Scott A. Jenkins received the B.S. degree in chemistry and physics from Yale University, New Haven, CT, in 1972 and the Ph.D. degree in oceanography from the Scripps Institution of Oceanography, University of California at San Diego, La Jolla, in 1980.

He is currently a Principal Engineer at the Marine Physical Laboratory of Scripps Institution of Oceanography. He is a Researcher in a nearshore physical oceanography and coastal engineering with experience in both field measurements, experimental design, and theoretical modeling. He has worked on a broad range of problems in coastal processes, including estuarine and littoral sediment transport, beach equilibrium and shoreline erosion, wave/structure interaction, hydrodynamic and hydraulic modeling of estuarine and harbor circulation, pollution dispersion modeling, and development of sedimentation control techniques. He holds four United States patents for sedimentation control devices.

Dr. Jenkins received the 1985 Inventor of the Year Award from the Patent Law Association and was the Co-Recipient of the 1988 Best Special Project Award from the American Council of Consulting Engineers.

Douglas L. Inman received the B.A. degrees in physics and geology from California State University, San Diego, in 1942, the M.S. degree in electric engineering from Harvard University, Cambridge, MA, in 1943, and the M.S. and Ph.D. degrees in oceanography from the University of California, Los Angeles, in 1948 and 1953, respectively.

He is a Research Professor of Oceanography and founding Director of the Center for Coastal Studies at Scripps Institution of Oceanography, University of California at San Diego, La Jolla. During his career, he and his students have pioneered the fields of nearshore and coastal processes. Their research provides the physical-mathematical relations that underlie the modeling of coastal morphology. He is the author of over 200 scientific publications.

Dr. Inman is a Guggenheim Fellow, and he has served as a UNESCO Lecturer in Marine Science in a number of countries. He was the Technical Director for the Orbit Award-Winning Film, *The Beach: A River of Sand*, and he has received the American Society of Civil Engineers International Coastal Engineering Award (1988) and the Ocean Science Educator Award (1990) from the U.S. Office of Naval Research.

Michael D. Richardson received the B.S. degree in oceanography from the University of Washington, Seattle, in 1967, the M.S. degree in marine science from the College of Williams and Mary, Williamsburg, VA, in 1971, and the Ph.D. degree in oceanography from the Oregon State University, Corvallis, in 1976.

He began working at the U.S. Naval Ocean Research and Development Activity, now part of the Naval Research Laboratory (NRL), Stennis Space Center, MS, in 1977. Except for a five-year assignment as a Principle Scientist at NATO's SACLANTCEN, La Spezia, Italy (1985–1989), he has worked at NRL as a Research Scientist and is currently the Head of the Seafloor Sciences Branch in the Marine Geosciences Division. His research interests include the effects of biological and physical processes on sediment structure, behavior, and physical properties near the sediment-water interface. His current research is linked to high-frequency acoustic scattering from and propagation within the seafloor and prediction of mine burial.

Dr. Richardson is a Fellow in the Acoustical Society of America, and a member of the American Geophysical Union (AGU), the European Geophysical Society, and Sigma Xi.

Thomas F. Wever received the Diploma degree in geophysics and the Ph.D. degree in field of continental crustal studies using reflection seismic methods, both from the Christian-Albrechts-Universität, Kiel, Germany, in 1985 and 1988, respectively.

He spent two months with PRAKLA-SEISMOS (now part of Schlumberger), Hannover, Germany, during his studies at the university and three semesters at Ludwig-Maximilians-Universität, Munich, Germany. Since 1990, he has been a Research Scientists at the Forschungsanstalt der Bundeswehr für Wasserschall und Geophysik (FWG), Kiel, Germany. He started in the field of sonar range prediction and, since 1992, has been working in the field of mine burial prediction and seafloor studies.

Dr. Wever is a member of the American Geophysical Union (AGU) and the European Association of Geoscientists and Engineers (EAGE).

Joseph Wasyl received the B.A. degree in biochemistry from the University of California at San Diego, La Jolla, in 1980.

He joined the staff of the Center for Coastal Studies, University of California at San Diego, as a Research Associate. He then transferred to the Development Engineering series, and is presently an Associate Development Engineer at the Marine Physical Laboratory, Scripps Institution of Oceanography. His main areas of expertise are mechanical engineering design and the computer modeling of estuarine and harbor circulation, pollution dispersion, shoreline erosion, wave/structure interaction, and estuarine and littoral sediment transport.